COMMUNICATIONS PHYSICS

ARTICLE

DOI: 10.1038/s42005-018-0028-1 OPEN

Tilted vortex cores and superconducting gap anisotropy in 2H-$NbSe_2$

J.A. Galvis[1,2], E. Herrera[1,2], C. Berthod[3], S. Vieira[1], I. Guillamón[1] & H. Suderow[1]

The superconductor 2H-$NbSe_2$ features vortices with a sixfold star shape when the magnetic field is applied perpendicular to the plane of the hexagonal crystal structure. This is due to the anisotropy in the quasi-two-dimensional Fermi surface tubes oriented along the *c* axis. But the properties of another, three-dimensional, pocket are unknown, in spite that it has a dominant contribution in many experiments. Here we measure vortices in tilted magnetic fields using a scanning tunneling microscope. We find patterns of stripes due to in-plane vortices and show how these change with the in-plane direction of the magnetic field. The shape of outgoing vortices is successfully compared with detailed calculations of vortex cores. Our data show that vortices exit at an angle with the surface and that the sixfold gap anisotropy is present over the whole Fermi surface.

[1] Laboratorio de Bajas Temperaturas y Altos Campos Magnéticos, Unidad Asociada UAM/CSIC, Departamento de Física de la Materia Condensada, Instituto de Ciencia de Materiales Nicolás Cabrera, Center for Condensed Matter Physics (IFIMAC), Universidad Autónoma de Madrid, E-28049 Madrid, Spain. [2] Facultad de Ingeniería y Ciencias Básicas, Universidad Central, Bogotá 110311, Colombia. [3] Department of Quantum Matter Physics, University of Geneva, 24 quai Ernest-Ansermet, 1211 Geneva, Switzerland. Correspondence and requests for materials should be addressed to C.B. (email: christophe.berthod@unige.ch) or to H.S. (email: hermann.suderow@uam.es)

The superconducting compound 2H-$NbSe_2$ has been considered for a long time as a prototypical example of a material with anisotropic superconducting properties – for instance, the upper critical field is three times larger when the field is applied in-plane than when it is perpendicular to the planes of the hexagonal crystalline structure[1]. The Fermi surface of 2H-$NbSe_2$ has two tubes around the Γ and K points due to bands derived from Nb orbitals which are nearly two-dimensional and a small three-dimensional pocket centered on the Γ point due to bands derived from Se orbitals[1–5]. A charge density wave (CDW) opens below 30 K in 2H-$NbSe_2$, coexisting with superconductivity below $T_c = 7.2$ K[4]. Scanning Tunneling Microscopy (STM) measurements in magnetic fields perpendicular to the hexagonal planes provide Density of States (DOS) maps giving sixfold vortex cores and the atomic scale tunneling conductance has a sixfold modulation[6–10]. Photoemission experiments suggest that the CDW induces the sixfold anisotropic superconducting gap[3,4]. This is reinforced by STM measurements on the superconducting gap in the isostructural compound 2H-NbS_2, which has a similar T_c and no CDW and is isotropic in-plane[11].

Photoemission experiments also suggest that the superconducting gap anisotropy is located in the Nb tubes and do not address the three dimensional Se-derived band[3,4]. On the other hand, penetration depth studies show that the gap at the Se sheet is large[12]. Furthermore, the Se sheet plays an essential role in most tunneling experiments[5]. Tunneling occurs preferentially through the last layer that consists of the hexagonal Se atom lattice[5,13]. It is however yet unclear what is the contribution of the electronic properties derived from Se to the superconducting gap anisotropy. To study this issue, measurements of the vortex core shape on a surface perpendicular to the *c* axis would be useful. However, no vortex imaging can then be made, because the surface is highly irregular due to the sheet-like structure of samples of 2H-$NbSe_2$. We study in this work the usual surface of 2H-$NbSe_2$, but we apply tilted magnetic fields.

Hess et al. measured the vortex lattice of 2H-$NbSe_2$ with STM in tilted magnetic fields[14,15]. They focused on the structure of the vortex lattice and found a distortion of the hexagonal lattice compatible with the anisotropy of the upper critical field, as well as a rotation of the orientation of the vortex lattice that is consistent with the anisotropic London theory[16–18]. When the magnetic field was close to being parallel to the hexagonal planes, they observed elongated vortex cores, instead of the sixfold cores seen in perpendicular fields, and a peculiar pattern of stripes. More recently, this pattern of stripes was addressed in STM measurements with the field exactly in-plane focusing on the influence of the structure of the vortex lattice and of screening currents[19,20]. Until now, there is no systematic study of the vortex core shape with the in-plane direction of the magnetic field and the relation of the observed stripe pattern with vortex core states remains unclear.

Here we visualize the DOS patterns and perform a detailed study as a function of the direction and bias voltage and show, thanks to a slight misorientation of the sample when the magnetic field is parallel to the surface, that the pattern of stripes is due to bound states of subsurface vortices. Furthermore, we find that the pattern changes between a two-fold vs. three-fold structure depending on the direction of the in-plane magnetic field with respect to the crystalline direction in the hexagonal plane. The images strongly change with the bias voltage, with the stripes disappearing when reaching the gap edge. We perform microscopic calculations of the DOS maps and their bias voltage dependence and find that the shape of in-plane vortex cores depends on the direction of the magnetic field with respect to the in-plane crystal lattice direction.

Results

Vortex lattice in tilted magnetic fields. In Fig. 1a we show the vortex lattice at 0.6 T with varying polar angle θ. The magnetic field is tilted at a fixed azimuthal angle $\varphi = 0°$, along an in-plane crystalline axis. That is, along the nearest neighbor axis in the hexagonal plane of the atomic surface plane (given by Se atoms, see Supplementary Note 2 and refs. [8,10]). For all tilts we observe a peak in the tunneling conductance due to Caroli–de Gennes–Matricon bound states at the center of the vortex cores, similar to the one observed at perpendicular magnetic fields[6–8,10]. However, there are remarkable differences in tilted fields.

The vortex core as observed in the zero bias tunneling conductance maps continuously increases its size when tilting the magnetic field (see also Supplementary Note 2) and acquires a two-fold shape at nearly in-plane magnetic fields. For these high tilt angles, we observe a pattern of stripes in the zero bias tunneling conductance maps (Fig. 1b).

In Fig. 1c we show the bias-voltage dependence of the tunneling conductance when crossing a stripe. We start from a gapped behavior in-between vortices and observe a small zero-bias peak when we cross the stripe. The zero-bias peak splits into two peaks at nonzero bias when leaving the center of the stripe (Fig. 1c inset, see also Supplementary Fig. 3), as expected for Caroli—de Gennes—Matricon bound states[6–8,10]. Thus, the stripes result from vortex-core bound states from subsurface vortices oriented along the tilt direction. Accordingly, the stripes always follow the direction of the magnetic field.

In addition, the pattern of stripes changes with the in-plane azimuthal angle φ with respect to the in-plane hexagonal crystal lattice. For the field along a crystal axis, $\varphi = 0°$ (left panel of Fig. 1b), the amount of stripes is about half the amount of stripes observed for $\varphi = 30°$ (right panel of Fig. 1b, this is at 90° (or equivalently at 30°) from the nearest neighbor Se–Se direction of the surface atomic lattice, see Supplementary Note 3 and refs[8,10]). The distance between vortices in the bulk is about 90 nm for a parallel magnetic field of 0.6 T. In Fig. 1b (left panel), when the magnetic field is along a crystalline axis ($\varphi = 0°$), we obtain 90 nm for the average distance between stripes. On the other hand, when the tilt of the magnetic field is in between crystalline axis ($\varphi = 30°$), we observe an average distance between stripes of 40 nm, about half the value found for $\varphi = 0°$ (Fig. 1b, right panel). This suggests that there is one stripe per in-plane vortex for $\varphi = 0°$, but two stripes for $\varphi = 30°$ per in-plane vortex. We can understand this if we consider that the in-plane vortex has a star shape, whose orientation changes with φ. As we will see below, a sixfold star vortex core whose shape is locked to the crystal lattice can provide such a behavior.

Vortex core in tilted magnetic fields. In Fig. 2 we compare the bias voltage dependence in perpendicular and tilted fields. In perpendicular magnetic fields, when increasing the bias voltage, we observe the same behavior as reported previously, showing the star shaped DOS associated to the in-plane anisotropy of the superconducting gap[8,10]. In tilted magnetic fields, the bias voltage dependence of the conductance maps is completely modified. The stripes observed at zero bias are no longer seen at higher bias (middle and right panels in Fig. 2). Instead, we observe broad dark-bright patterns along the tilt of the magnetic field.

Note that the images show several outgoing vortices, in addition to the stripes. Note also that this is very different from the observations made in refs[19,20] (at a single bias voltage and azimuthal angle and as a function of the value of the magnetic field) which show just stripes and no vortices. In our data, from the vortex density we obtain $\theta = 87.5°$ in Fig. 1b left panel (and in Fig. 2 middle column), and $\theta = 85.6°$ in Fig. 1b right panel (and in

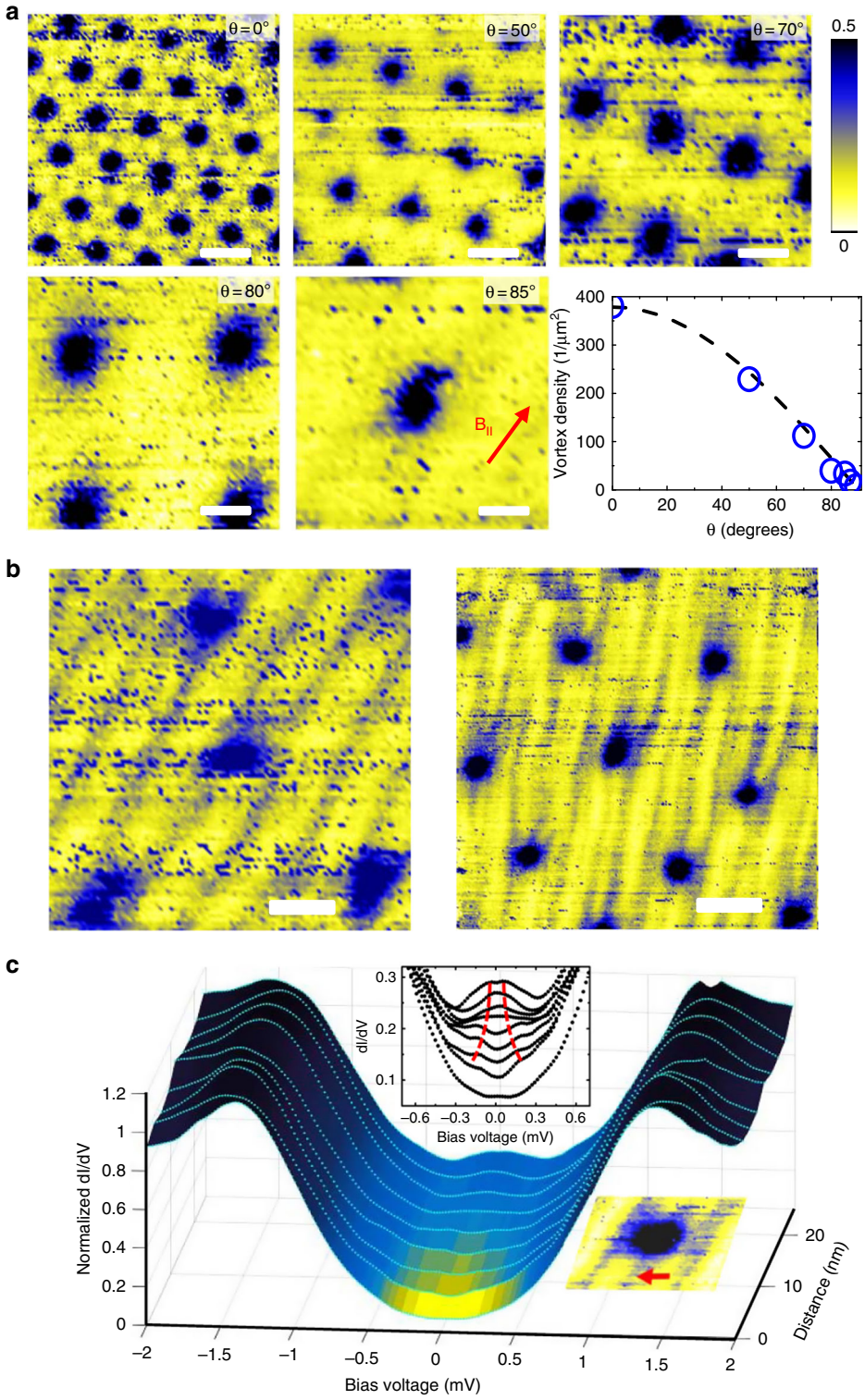

Fig. 1 Tilted vortex cores. **a** The vortex lattice as a function of the polar angle (θ) at 0.6 T with azimuthal angle $\varphi = 0°$. Maps trace the zero-bias normalized conductance (normalized conductance units, NCU). Scale bar = 50 nm. In the lower right panel we show the vortex density (blue points) compared with expectations taking into account the anisotropy of the upper critical field (dashed line, see Supplementary Note 1)[16]. **b** Maps with polar angle close to $\theta =$ 90° for two different azimuthal angles $\varphi = 0°$ (left panel) and $\varphi = 30°$ (right panel). There is a small uncertainty in θ, which produces outgoing vortices and a pattern of stripes. Color scale of both figures is the same as in **a**. **c** The normalized tunneling conductance curves when crossing a stripe are shown in the main panel. Bottom curves are tunneling conductance data outside the stripe and top curves at the center of the stripe. In the lower right inset we show a zero bias conductance image with an outgoing vortex and the stripes. The red arrow provides the path giving the set of tunneling conductance curves of the main panel. Upper inset shows a zoom of the evolution of the conductance close to zero bias, with a dashed red line marking the splitting of the zero-bias peak. All data are taken at $T = 150$ mK

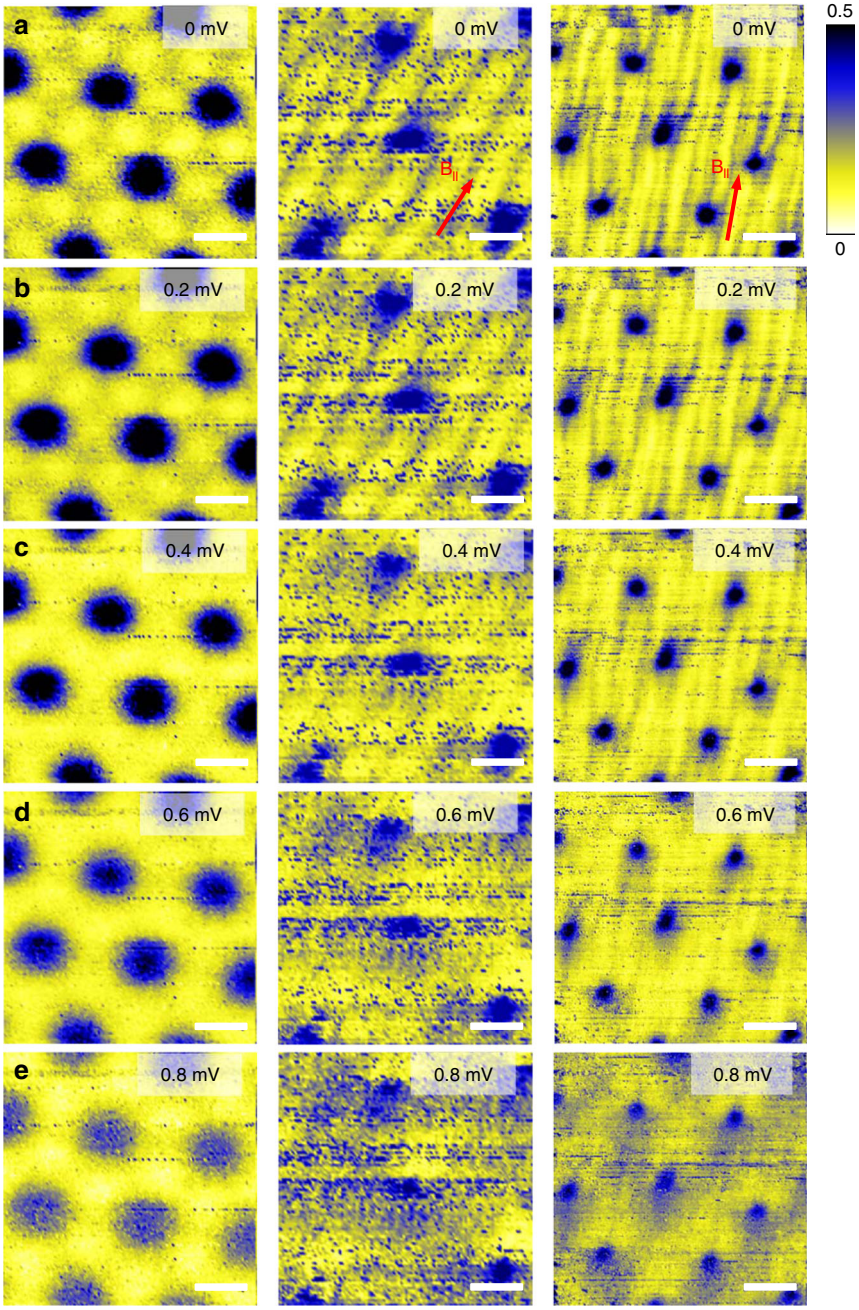

Fig. 2 Tilted vortex cores vs. bias voltage. In **a**–**e** we show conductance maps for bias voltages of 0 mV (**a**), 0.2 mV (**b**), 0.4 mV (**c**), 0.6 mV (**d**), 0.8 mV (**e**). Left panels show conductance maps with a field of 0.6 T parallel to the *c* axis. Middle and right panels show conductance maps at nearly parallel magnetic fields ($\theta \approx 90°$ with an uncertainty of a few degrees). In the middle panels, the in-plane tilt is with the azimuthal angle along a crystalline direction ($\varphi = 0$) and in the right panels in between crystalline directions ($\varphi = 30°$). The in-plane direction of the tilt is shown by the red arrows in middle and right panels of **a**. Scale bars are of 30 nm in the left panels and 120 nm in middle and right panels. The color scale is given by the bar in **a**. The vortex density decreases for nearly parallel magnetic fields. The stripes at mostly visible at zero bias and follow the in-plane direction of the magnetic field in **a**. At high bias, the stripes are no longer present. Vortices present elongated shapes and are strongly in-plane asymmetric, with a clear yellow-blue pattern along the in-plane direction of the magnetic field (**e**, middle and right panels).

Fig. 2 right column). These angles are within the possible misorientation with respect to a parallel magnetic field that can be obtained in our experiment (see Methods section). As we discuss in detail below, vortices might come out either perpendicular or at an angle to the surface. The shape of the vortices we observe in highly tilted fields, as well as their bias voltage dependence, is totally different than the shape of vortices in perpendicular fields. Their structures actually merge into the stripes when leaving the vortex centers, having the same two vs. three fold structure of rays that extend into the stripes far from vortex cores. They are also, as remarked above, considerably larger than vortices in perpendicular fields. Thus, we are observing vortices exiting the surface at an angle.

DOS of vortex cores in tilted magnetic fields. To model such a situation, we perform microscopic calculations of tilted vortex cores in a superconductor with a sixfold gap anisotropy. It turns

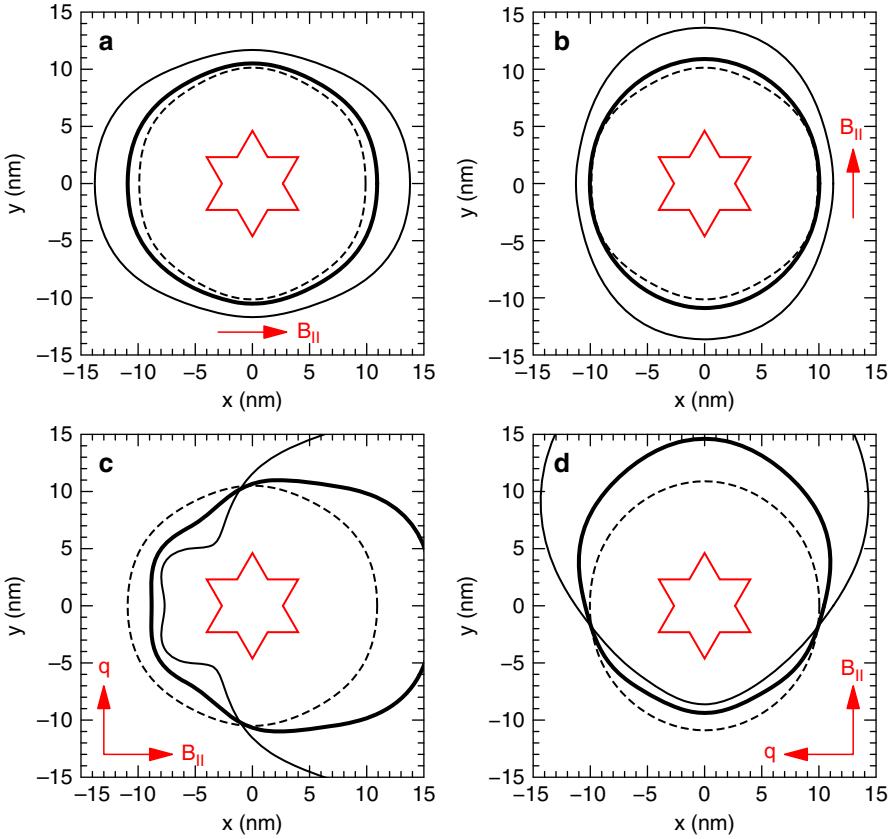

Fig. 3 Order parameter distribution for tilted vortex cores. Contours at a constant value of the order parameter are given for three values of the tilt of the magnetic field τ ($\tau = 0$: dashed; 0.5: thick; 1: thin) with (**a**) field tilted along the a axis ($\varphi = 0°$) and (**b**) field tilted perpendicular to the a axis ($\varphi = 30°$). **c** and (**d**) Results at $\tau = 0.5$ for three values of q ($qa = 0$: dashed; 0.004: thick; 0.008: thin, a being the lattice parameter) for $\varphi = 0°$ and 30°, respectively. The shape of the vortex core from the zero bias tunneling conductance in perpendicular fields is schematically marked by the red star for reference

out that it is a formidable task to calculate the vortex core shape in tilted magnetic fields because one needs to obtain the DOS as a function of the position in three-dimensional space with a high spatial accuracy and then analyze the magnetic field and gap structure as a function of the tilt. This has never been achieved, to our knowledge. We start by building DOS maps of isolated vortices in an effective two-dimensional model (Supplementary Note 4) and calculate the DOS maps as a function of energy and the azimuthal angle of the magnetic field (Supplementary Note 5). We simulate a vortex tilted to the hexagonal plane by a two-fold distribution of the supercurrent along the tilt, using calculations of ref. [21]. We introduce in addition a shift q in the condensate momentum to account for the current distribution due to the in-plane vs. out-of-plane crystalline anisotropy (Supplementary Note 5). In Fig. 3 we show the vortex-core shape from contours of constant order parameter around the vortex cores when tilting the magnetic field (a and b) with zero q and with nonzero q (c and d). With zero q, we see that the DOS pattern becomes elliptical. With a finite q we find that the DOS map of the vortex core develops a comet like shape, increasing considerably its size along the tilt of the magnetic field. The comet shape has a two-fold structure perpendicular to the tilt when the tilt is along a crystalline axis ($\varphi = 0°$) and a triangular form when the tilt is at 30° to a crystalline axis ($\varphi = 30°$).

In Fig. 4 we show the energy dependence of the DOS with the field tilted along the nearest-neighbor direction of the vortices and perpendicular to this direction (middle and right columns, respectively). We see that the vortex core shape obtained from the DOS is highly energy dependent. The spatial extension of the DOS around a vortex core is considerably larger in tilted fields. This is consistent with the observed increase in the vortex core size in the tunneling conductance when comparing maps made at perpendicular field with maps at nearly parallel fields (Fig. 1a). For energies close to the gap edge, at 0.8 meV the spatial extension is considerably reduced and has more structure.

Note that the model addresses a single vortex. Stripes result from vortex cores lying in-plane that reach the surface. Stripes of neighboring subsurface vortices extend to the surface and join each other. The shape of the order parameter extends along directions that change with the azimuthal angle φ (Fig. 3), indicating that along these directions states of neighboring vortices overlap and lead to the observed stripes. In Fig. 3c we observe that the vortex extends preferentially along its sides, leading to the two-fold structure seen in the left panel of Fig. 1b. In Fig. 3d (Fig. 1b, right panel), we observe instead that the vortex core extends along the tilt and its sides, leading to the additional stripe exiting from the center of vortex cores in the right panel of Fig. 1b.

Note also that the model reproduces features of the bias voltage dependence of vortices exiting the surface at an angle. In particular, the increase of the DOS along the tilt for zero bias reverses for high bias. We can take in Fig. 4 the phase singularity (white point) as a reference to compare DOS maps for different bias. The tunneling conductance is high (bluish, high DOS) at low bias, but lower (yellowish, low DOS) at high bias along the direction of the magnetic field. Similarly, the vortices observed in Fig. 2 (middle and right columns) change their two-fold shape along the in-plane magnetic field.

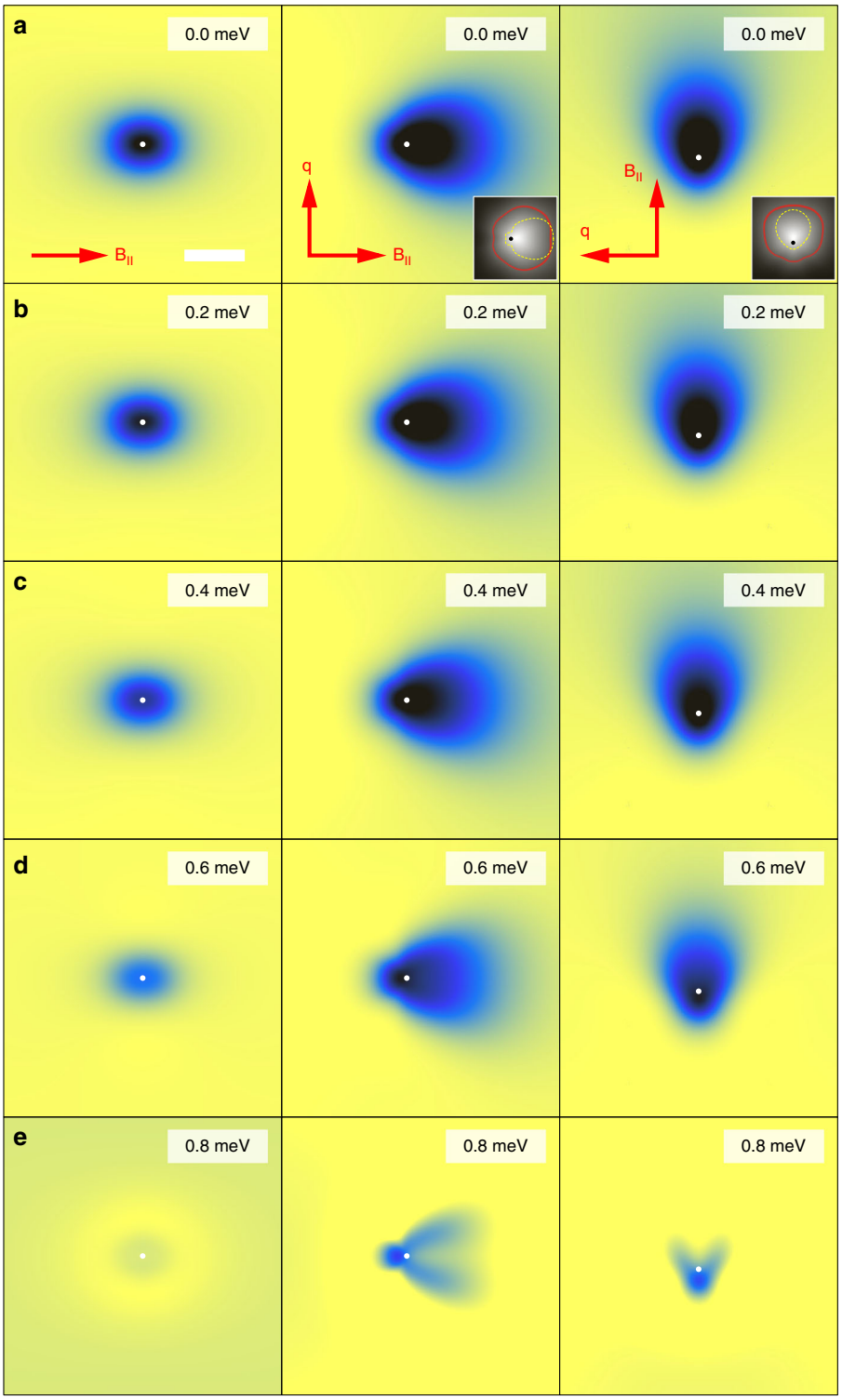

Fig. 4 Calculated tilted vortex core shape vs. energy. We show calculated DOS patterns as a function of the energy (**a** at 0 meV, **b** at 0.2 meV, **c** at 0.4 meV, **d** at 0.6 meV, **e** at 0.8 meV). In the left panels we show the DOS of a vortex with the field tilted along the a axis ($\varphi = 0°$, x-axis of the panels), calculated without taking into account surface currents. In the middle and right panels we show the result taking into account surface currents when the in-plane tilt is $\varphi = 0°$ (middle panels) and $\varphi = 30°$ (right panels). The current is of $qa = 0.008$ in both cases. The direction of in-plane magnetic field and current is shown by the red arrows in **a**. The scale bar is shown in the left panel of (**a**) and is the same for all panels, of 30 nm size. The color map goes from yellow (minimum DOS) to the zero bias peak in the DOS in black. The white dots in each panel show the phase singularity point. The tilt strength is $\tau = 0.5$ in all panels. Insets in middle and right panels of (**a**) display the core shape on a logarithmic gray scale together with the shape of the order parameter as an iso-contour of the DOS (red dashed lines) and an iso-contour of the DOS (red line).

Discussion

Vortices in tilted fields close to the surface are very different in 2H-$NbSe_2$ than in other materials. In the isotropic superconducting material $\beta-Bi_2Pd$, vortices at the surface have the same shape whatever the in-plane direction of the magnetic field[22]. On the other hand, highly anisotropic materials like cuprates show two-dimensional pancake vortices, with the same shape at the surface than for perpendicular fields[23,24]. In both cases, the vortex core in tilted magnetic fields just shows the anisotropic properties in the plane, either because vortices bend close to the surface in $\beta-Bi_2Pd$ or because vortices are fully confined within the layers (pancake vortices) in the cuprates. In 2H-$NbSe_2$ the observed DOS patterns are spatially highly structured at all bias voltages, indicating a more intricate situation.

In order to explain this situation, let us consider the energetics of vortices close to the surface in tilted magnetic fields and how this influences the three different systems mentioned here. We have to consider the balance between the elastic energy cost associated with vortex bending, which favors straight vortices exiting at an angle to the surface, and the cost associated with establishing strongly distorted current loops around vortices close to the surface which favors circular current loops and vortices exiting perpendicular to the surface[24,25].

The shear modulus c_{44} is given by $c_{44} \approx (1 + k^2\lambda^2)^{-1}$ with k being the wavevector for the distortion[25]. Close to the surface, the wavevector relevant for this problem is $k = 1/a$ where a is the bending radius. a is given by the minimum between the intervortex distance a_0 and the penetration depth λ[26]. For the magnetic fields considered here, a_0 is of about 90 nm, always smaller than λ, thus $a \approx a_0$. On the other hand, the current distribution surrounding the vortex is determined by the anisotropy of the upper critical field and is elliptical, with its short axis along the direction where the upper critical field is higher (and the coherence lengths smaller)[25,27,28].

In $\beta-Bi_2Pd$, vortices exiting the surface have a circular shape and bend close to the surface[22]. The shear modulus of the vortex lattice is isotropic and the lattice is sufficiently soft that it is energetically favorable to exit perpendicular to the surface for all tilts. The upper critical field in $\beta-Bi_2Pd$ is low (0.6 T) and the coherence length of about 20 nm, so that vortices are larger than in 2H-$NbSe_2$ and the cuprates and certainly round because the upper critical field is nearly isotropic[29,30]. In $\beta-Bi_2Pd$, $\lambda \approx 100$ nm, which increases the elastic energy associated with vortex bending close to the surface as compared to materials with larger λ[22,30]. However, this is balanced by the gain in establishing current loops parallel to the surface with bent vortices[21].

In the cuprates, tilted fields create arrangements of crossing pancake and Josephson vortex lattices whose structure strongly depends on the temperature, magnetic field and tilt[31–34]. Lattices of pancake vortices slightly shifted between layers can appear under some conditions, leading in essence to tilted lines of vortices that are expected to exit at an angle to the surface[21,35–37]. However, at least for materials in which the c-axis coherence length is below the interlayer distance, there is no reason for vortex bending as no Abrikosov vortices are established between layers. Current loops of Abrikosov vortices are parallel to the surface, and the balance is rather played by the interaction between Abrikosov and Josephson vortex lattices.

Here in 2H-$NbSe_2$, the upper critical field anisotropy is of a factor of three and the out of plane coherence length is well above the c-axis lattice constant[15,38,39]. This creates elliptical Abrikosov vortices (there are no Josephson vortices) with the short axis perpendicular to the surface. This helps establishing current loops close to the surface, as the vortex is anyhow shorter along the direction perpendicular to the surface. Tilted vortices can thus exit at an angle to the surface, neither parallel nor perpendicular to the surface. This leads to an intricate surface current pattern that modifies the vortex core shape at all bias, as shown by the vortices imaged in our experiment.

On the other hand, the appearance of stripes is also unique to 2H-$NbSe_2$. As we show above, this is due to subsurface vortex cores. The zero bias peak due to Caroli–de Gennes–Matricon states is indeed a characteristic feature of 2H-$NbSe_2$ and it extends indeed over distances far from the vortex core[7,8,10]. In our experiments, the distance between stripes from subsurface vortices is comparable to the intervortex distance expected for the applied in-plane magnetic field, with each subsurface vortex providing a different number of stripes, depending on the in-plane direction of the tilt, as shown in Fig. 1b and as discussed in connection with Fig. 3.

The combined appearance of stripes and vortices could be also due, in principle, to crossing perpendicular vortex and parallel vortex lattices[40]. Within such a situation, however, it seems quite difficult to obtain patterns of stripes with distances that change when varying the in-plane direction of the tilt.

We can conclude that the differences between 2H-$NbSe_2$, $\beta-Bi_2Pd$ and the cuprates are due to a totally different DOS pattern for parallel magnetic fields. The pattern results from subsurface vortex cores and provides access to the shape of in-plane vortices and thus to the gap anisotropy in the out-of-plane three-dimensional part of the Fermi surface.

The shape of the superconducting gap along the c axis should influence the dependence of the core shape with the in-plane direction of the tilt. As we show above, the main asymmetric features observed in our experiment and their dependence with the azimuthal angle can be explained by a sixfold anisotropic superconducting gap in 2H-$NbSe_2$. This shows that the sixfold gap anisotropy is spread over the whole Fermi surface.

It is useful to compare with the situation in MgB_2, where vortex cores have been studied for magnetic fields always applied perpendicular to the surface, but with surfaces out- as well as in-plane[41,42]. An elongated vortex core shape was expected for fields in-plane, due to the two-dimensional part of the Fermi surface[43]. This was however not observed. Vortices are round out- and in-plane, with their shape being dominated by the three-dimensional part of the Fermi surface, both the vortex core shape in the DOS[41–43] as well as in the magnetic field pattern[44]. It was concluded that tunneling is dominated in all cases by the three-dimensional part of the Fermi surface. Tunneling in 2H-$NbSe_2$ is also dominated by the three dimensional part of the Fermi surface, here due to the stronger contribution to tunneling of the Se orbitals[5]. However, the situation is quite different. Whereas the three-dimensional pocket amounts for the largest part of the DOS at the Fermi level in MgB_2, the Se pocket in 2H-$NbSe_2$ is small and amounts just for 20% of the DOS[5]. The gap anisotropy in 2H-$NbSe_2$ was until now just associated to the Nb two dimensional sheets. As we show here, the sixfold gap anisotropy remains out-of-plane, which suggests that it is present over the whole Fermi surface.

Interband interactions are strong in 2H-$NbSe_2$[5]. Although there are evidences for a two gap behavior from tunneling spectroscopy, penetration depth and thermal conductivity[5,10,12,45,46], the obtained spread in gap values is of a factor of 1.5 or at most 2. Our measurements suggest that interactions are such that the sixfold anisotropy in the shape of the superconducting gap is inherited from the Nb two-dimensional bands over to the whole Fermi surface.

STM in tilted magnetic fields is thus a sensitive probe of the superconducting electronic DOS, particularly in three-dimensional superconductors with strongly anisotropic and sharply defined vortex core bound states. The main advantage with respect to studying different crystalline surfaces is that the

direction of the magnetic field can be varied at will on a single surface. Efforts, still under development, have been also devoted to other techniques. Quasiparticle interference has been extended out of the surface plane by triangulating electronic wavefunctions from in-depth impurities or studying inter and intraband scattering[47–52]. Macroscopic specific heat and thermal conductivity measurements in rotating fields have been also performed with the aim to obtain the anisotropy of the superconducting gap[53]. These provide the spatially averaged DOS and are influenced by scattering effects, whereas STM provides directly the spatially resolved electronic DOS, i.e. in and around vortex cores.

Methods

Model and calculations. We create a microscopic model with a sixfold anisotropic superconducting gap, by a triangular lattice and a tight-binding dispersion (see Supplementary Notes 4,5 for more information). To calculate the spatial dependence of the superconducting DOS we need a very large system size. In the low-energy region the inter-level spacing is $\Delta E \sim \hbar v_F \Delta k$ with $\Delta k = 2\pi/(Na)$, where Na is the linear system size. In order to reach a resolution $\Delta E \lesssim \sim 1$ meV of the order of the superconducting gap, a total number of unit cells $N^2 \gtrsim 200\,000$ is required. This sets the size of the Bogoliubov-de Gennes Hamiltonian to at least 400,000 × 400,000. Straight diagonalization is therefore not an option. Instead we use the method described in ref. [54], the DOS is expanded on Chebyshev polynomials of the Hamiltonian and can thus be evaluated iteratively with low memory cost, even for very large systems. We use a finite lattice made of M concentric hexagons surrounding the site where the DOS is calculated. To reach the desired accuracy we perform the calculation with $M = 1000$, corresponding to a lattice of 3 003 001 sites. The Chebyshev expansion is truncated at order $4M$ and terminated using the Jackson kernel[55,56]. To obtain results in an applied magnetic field and as a function of position and energy we use a Lawrence-Doniach model following ref. [21]. We are not aware of an equivalent model for vortex lattices – hence we consider only isolated vortices. In Supplementary Note 5 we solve the nonlinear model of ref. [21] to leading order in the tilt angle and get an analytical expression for the phase. The distortion is proportional to the tilt strength defined as $\tau = \xi_{ab}^2/(2\xi_c^2)\tan^2\theta$, with θ being the polar angle. The DOS maps and anisotropies of the order-parameter are determined self-consistently as a function of τ. We use tilt strengths of $\tau \approx 0.5$, which correspond to small $\theta \approx 15°$. We believe that this accounts well for our situation, with a three dimensional, strongly anisotropic superconductor. To further address this anisotropy, we introduce an additional phase in the order parameter, i.e., $\Phi(\mathbf{r}) \to \Phi(\mathbf{r}) - \mathbf{q}\cdot\mathbf{r}$, with q being a surface current. We take q up to about one third of the value corresponding to the critical current.

STM methods. We use a setup described in ref. [57] which consists of a dilution refrigerator with a STM thermally anchored to the mixing chamber reaching temperatures of 150 mK. The STM is located at the center of a three axis magnet. The three axis magnet consists of a long solenoid providing the z-axis magnetic field and a pair of split coils for x- and y-axis magnetic field components. We estimate the accuracy in the determination of the azimuthal and polar angles θ and φ at the magnetic fields used here (of order of a Tesla) to be about 4–5°. This uncertainty is composed of a slight misalignment of the surface of the sample with respect to the coil system and of remanent magnetic fields inside the coils, that can be in the range of the mT. We measure high quality 2H-$NbSe_2$ samples grown using the usual iodine vapor transport method. The in-plane tilt direction is corrected to obtain values for φ that are fixed to the atomically resolved hexagonal Se lattice obtained by STM imaging (see also Supplementary Fig. 5). We take tunneling conductance maps as a function of the bias voltage, as usual in vortex imaging using STM. Sample surface has been prepared by cleaving and the Au tip is prepared using a pad of Au as described in ref. [58].

Data availability. The datasets generated during the current study are available at https://osf.io/uhgpf/ DOI 10.17605/OSF.IO/UHGPF.

Received: 10 December 2017 Accepted: 18 May 2018
Published online: 27 June 2018

References

1. Corcoran, R. et al. Quantum oscillations in the mixed state of the type II superconductor 2H-$NbSe_2$. *J. Phys. Condens. Mat.* **6**, 4479–4492 (1994).
2. Janssen, T. J. B. M. et al. Quantitative investigation of the de Haas-van Alphen effect in the superconducting state. *Phys. Rev. B* **57**, 11698–11712 (1998).
3. Kiss, T. et al. Charge-order-maximized momentum-dependent superconductivity. *Nat. Phys.* **3**, 720–725 (2007).
4. Rahn, D. J. et al. Gaps and kinks in the electronic structure of the superconductor 2H-$NbSe_2$ from angle-resolved photoemission at 1K. *Phys. Rev. B* **85**, 224532 (2012).
5. Johannes, M. D., Mazin, I. I. & Howells, C. A. Fermi-surface nesting and the origin of the charge-density wave in 2H-$NbSe_2$. *Phys. Rev. B* **73**, 205102 (2006).
6. Caroli, C., de Gennes, P. G. & Matricon, J. Bound fermion states on a vortex line in a type II superconductor. *Phys. Lett.* **9**, 307–309 (1964).
7. Hess, H. F., Robinson, R. B., Dynes, R. C., Valles, J. M. & Waszczak, J. V. Scanning-tunneling-microscope observation of the Abrikosov flux lattice and the density of states near and inside a fluxoid. *Phys. Rev. Lett.* **62**, 214–216 (1989).
8. Hess, H. F., Robinson, R. B. & Waszczak, J. V. Vortex-core structure observed with a scanning tunneling microscope. *Phys. Rev. Lett.* **64**, 2711–2714 (1990).
9. Hayashi, N., Isoshima, T., Ichioka, M. & Machida, K. Low-lying quasiparticle excitations around a vortex core in quantum limit. *Phys. Rev. Lett.* **80**, 2921–2924 (1998).
10. Guillamón, I., Suderow, H., Guinea, F. & Vieira, S. Intrinsic atomic-scale modulations of the superconducting gap of 2H-$NbSe_2$. *Phys. Rev. B* **77**, 134505 (2008).
11. Guillamón, I. et al. Superconducting density of states and vortex cores of 2H-NbS_2. *Phys. Rev. Lett.* **101**, 166407 (2008).
12. Fletcher, J. D. et al. Penetration depth study of superconducting gap structure of 2H-$NbSe_2$. *Phys. Rev. Lett.* **98**, 057003 (2007).
13. Noat, Y. et al. Quasiparticle spectra of 2H-$NbSe_2$: two-band superconductivity and the role of tunneling selectivity. *Phys. Rev. B* **92**, 134510 (2015).
14. Hess, H. F., Murray, C. A. & Waszczak, J. V. Scanning-tunneling-microscopy study of distortion and instability of inclined flux-line-lattice structures in the anisotropic superconductor 2H-$NbSe_2$. *Phys. Rev. Lett.* **69**, 2138–2141 (1992).
15. Hess, H. F., Murray, C. A. & Waszczak, J. V. Flux lattice and vortex structure in 2H-$NbSe_2$ in inclined fields. *Phys. Rev. B* **50**, 16528–16540 (1994).
16. Campbell, L. J., Doria, M. M. & Kogan, V. G. Vortex lattice structures in uniaxial superconductors. *Phys. Rev. B* **38**, 2439–2443 (1988).
17. Gammel, P. L. et al. Small angle neutron scattering study of the magnetic flux-line lattice in single crystal 2H-$NbSe_2$. *Phys. Rev. Lett.* **72**, 278–281 (1994).
18. Kogan, V. G., Bulaevskii, L. N., Miranović, P. & Dobrosavljević-Grujić, L. Vortex-induced strain and flux lattices in anisotropic superconductors. *Phys. Rev. B.* **51**, 15344–15350 (1995).
19. Fridman, I., Kloc, C., Petrovic, C. & Wei, J. Y. T. Lateral imaging of the superconducting vortex lattice using Doppler-modulated scanning tunneling microscopy. *Appl. Phys. Lett.* **99**, 192505 (2011).
20. Fridman, I., Kloc, C., Petrovic, C. & Wei, J. Y. T. Observation of an in-plane vortex lattice transition in the multiband superconductor 2H-$NbSe_2$ using scanning tunneling spectroscopy. *arXiv:1303.3559* (2013).
21. Bulaevskii, L. N., Ledvij, M. & Kogan, V. G. Vortices in layered superconductors with Josephson coupling. *Phys. Rev. B* **46**, 366–380 (1992).
22. Herrera, E. et al. Subsurface bending and reorientation of tilted vortex lattices in bulk isotropic superconductors due to Coulomb-like repulsion at the surface. *Phys. Rev. B* **96**, 184502 (2017).
23. Beleggia, M. et al. Model of superconducting vortices in layered materials for the interpretation of transmission electron microscopy images. *Phys. Rev. B* **70**, 184518 (2004).
24. Kogan, V. G. & Kirtley, J. R. Determining the vortex tilt relative to a superconductor surface. *Phys. Rev. B* **96**, 174516 (2017).
25. Brandt, E. H. The flux-line lattice in superconductors. *Rep. Prog. Phys.* **58**, 1465–1594 (1995).
26. Brandt, E. H. Tilted and curved vortices in anisotropic superconducting films. *Phys. Rev. B* **48**, 6699–6702 (1993).
27. Blatter, G., Feigel'man, M. V., Geshkenbein, V. B., Larkin, A. I. & Vinokur, V. M. Vortices in high-temperature superconductors. *Rev. Mod. Phys.* **66**, 1125–1388 (1994).
28. Kogan, V. G., Nakagawa, N. & Thiemann, S. L. Interaction of vortices in uniaxial superconductors. *Phys. Rev. B* **42**, 2631–2634 (1990).
29. Herrera, E. et al. Magnetic field dependence of the density of states in the multiband superconductor $\beta - Bi_2Pd$. *Phys. Rev. B* **92**, 054507 (2015).
30. Kačmarčík, J. et al. Single-gap superconductivity in β–Bi_2Pd. *Phys. Rev. B* **93**, 144502 (2016).
31. Vlasko-Vlasov, V. K., Glatz, A., Koshelev, A. E., Welp, U. & Kwok, W. K. Anisotropic superconductors in tilted magnetic fields. *Phys. Rev. B* **91**, 224505 (2015).
32. Koshelev, A. E. Crossing lattices, vortex chains, and angular dependence of melting line in layered superconductors. *Phys. Rev. Lett.* **83**, 187–190 (1999).
33. Vlasko-Vlasov, V. et al. Flux cutting in high-T_c superconductors. *Phys. Rev. B* **91**, 014516 (2015).
34. Bending, S. Local magnetic probe of superconductors. *Adv. Phys.* **48**, 449–535 (1999).

35. Tonomura, A. et al. Observation of structures of chain vortices inside anisotropic high-T_c superconductors. *Phys. Rev. Lett.* **88**, 237001 (2002).
36. Koshelev, A. E. Kink walls and critical behavior of magnetization near the lock-in transition in layered superconductors. *Phys. Rev. B* **48**, 1180–1191 (1993).
37. Tonomura, A. et al. Observation of individual vortices trapped along columnar defects in high-temperature superconductors. *Nature* **412**, 620–622 (2001).
38. Foner, S. & McNiff, E. Upper critical fields of layered superconducting $NbSe_2$ at low temperature. *Phys. Lett. A* **45**, 429–430 (1973).
39. Nader, A. & Monceau, P. Critical field of 2H-$NbSe_2$ down to 50 mK. *Springer Plus* **3**, 16 (2014).
40. Daemen, L. L., Campbell, L. J., Simonov, A. Y. & Kogan, V. G. Coexistence of two flux-line species in superconducting slabs. *Phys. Rev. Lett.* **70**, 2948–2951 (1993).
41. Eskildsen, M. R. et al. Vortex imaging in the π band of magnesium diboride. *Phys. Rev. Lett.* **89**, 187003 (2002).
42. Eskildsen, M. R. et al. Vortex imaging in magnesium diboride with $H\perp c$. *Phys. Rev. B* **68**, 100508 (2003).
43. Ichioka, M., Machida, K., Nakai, N. & Miranović, P. Electronic state around vortex in a two-band superconductor. *Phys. Rev. B* **70**, 144508 (2004).
44. Loudon, J. C., Yazdi, S., Kasama, T., Zhigadlo, N. D. & Karpinski, J. Measurement of the penetration depth and coherence length of 2H-$NbSe_2$ in all directions using transmission electron microscopy. *Phys. Rev. B* **91**, 054505 (2015).
45. Boaknin, E. et al. Heat conduction in the vortex state of 2H-$NbSe_2$: Evidence for multiband superconductivity. *Phy. Rev. Lett.* **90**, 117003 (2003).
46. Rodrigo, J. G. & Vieira, S. STM study of multiband superconductivity in 2H-$NbSe_2$ using a superconducting tip. *Phys. C* **404**, 306–310 (2004).
47. Hoffman, J. E. Spectroscopic scanning tunneling microscopy insights into Fe-based superconductors. *Rep. Prog. Phys.* **74**, 124513 (2011).
48. Petersen, L. et al. Direct imaging of the two-dimensional Fermi contour: Fourier-transform STM. *Phys. Rev. B* **57**, R6858–R6861 (1998).
49. Hoffman, J. E. et al. A four unit cell periodic pattern of quasi-particle states surrounding vortex cores in $Bi_2Sr_2CaCu_2O_{8+\delta}$. *Science* **295**, 466–469 (2002).
50. Simon, L., Bena, C., Vonau, F., Cranney, M. & Aubel, D. Fourier-transform scanning tunnelling spectroscopy: the possibility to obtain constant-energy maps and band dispersion using a local measurement. *J. Phys. D.* **44**, 464010 (2011).
51. Weismann, A. et al. Seeing the Fermi surface in real space by nanoscale electron focusing. *Science* **323**, 1190–1193 (2009).
52. Ruby, M., Heinrich, B. W., Pascual, J. I. & Franke, K. J. Experimental demonstration of a two-band superconducting state for lead using scanning tunneling spectroscopy. *Phys. Rev. Lett.* **114**, 157001 (2015).
53. Matsuda, Y., Izawa, K. & Vekhter, I. Nodal structure of unconventional superconductors probed by angle resolved thermal transport measurements. *J. Phys. Condens. Mat.* **18**, R705–R752 (2006).
54. Covaci, L., Peeters, F. M. & Berciu, M. Efficient numerical approach to inhomogeneous superconductivity: the Chebyshev-Bogoliubov-de Gennes method. *Phys. Rev. Lett.* **105**, 167006 (2010).
55. Weisse, A., Wellein, G., Alvermann, A. & Fehske, H. The kernel polynomial method. *Rev. Mod. Phys.* **78**, 275–306 (2006).
56. Berthod, C. Vortex spectroscopy in the vortex glass: a real-space numerical approach. *Phys. Rev. B* **94**, 184510 (2016).
57. Galvis, J. A. et al. Three axis vector magnet set-up for cryogenic scanning probe microscopy. *Rev. Sci. Instrum.* **86**, 013706 (2015).
58. Suderow, H., Guillamón, I. & Vieira, S. Compact very low temperature scanning tunneling microscope with mechanically driven horizontal linear positioning stage. *Rev. Sci. Instrum.* **82**, 033711 (2011).

Acknowledgements

We acknowledge discussions with V.G. Kogan and J.R. Kirtley. Work done in Madrid was supported by the Spanish Ministry of Economy and Competitiveness (FIS2014-54498-R, MDM-2014-0377), by the Comunidad de Madrid through program Nanofrontmag-CM (S2013/MIT-2850), by EU (European Research Council PNICTEYES grant agreement 679080, FP7-PEOPLE-2013-CIG 618321 and COST Action CA16218) and by Axa Research Fund. SEGAINVEX-UAM is also acknowledged. We also acknowledge the support of Departamento Administrativo de Ciencia, Tecnologa e Innovacin, COLCIENCIAS (Colombia) Programa Doctorados en el Exterior Convocatoria 568-2012 and the Cluster de investigación en ciencias y tecnologías convergentes de la Universidad Central (Colombia). Work done in Geneva was supported by the Swiss National Science Foundation under Division II. Calculations were done in the University of Geneva with the clusters Mafalda and Baobab.

Author contributions

J.A.G. and E.H. performed the experiment with the help and supervision of I.G. and H.S. H.S. and I.G. designed the instrument, and managed, together with S.V. its set-up. I.G. proposed studying 2H-$NbSe_2$ and supervised interpretation of data. C.B. devised the method to obtain the spatial dependence of the density of states in the mixed state in tilted magnetic fields and performed the calculations. Results and manuscript were discussed by all authors.

Additional information

Supplementary information accompanies this paper at https://doi.org/10.1038/s42005-018-0028-1.

Competing interests: The authors have no conflicts of interest to disclose.